

Nomenclature

Acronyms / Abbreviations

1-D	One-Dimensional
AFM	Atomic Force Microscopy
AlN	Aluminium Nitride
BSE	Back Scattered Electron
BSF	Basal-plane Stacking Fault
C-AFM	Conductive Atomic Force Microscopy
EBL	Electron Blocking Layer
EL	Electroluminescence
ET	Electron Tomography
FIBT	Focussed Ion Beam Tomography
FSR	Free Spectral Range
GaAs	Gallium Arsenide
GaN	Gallium Nitride
InN	Indium Nitride
LED	Light-Emitting Diode
PD	Partial Dislocation
PSF	Prismatic Stacking Fault

SEM	Scanning Electron Microscope
SE	Secondary Electron
SPS	Single Photon Source
WGM	Whispering Gallery Mode

Chapter 2

Experimental Methods

2.1 Transmission Electron Microscopy

A typical transmission electron microscope (TEM) consists of a high voltage (typically 100-400kV) electron gun under extremely high vacuum conditions within a column. The beam of electrons generated by this gun passes through a set of lenses which focus or deflect the beam before it is incident on the sample under examination. If this sample is thin enough to be electron transparent, the electrons passing through it and scattering elastically or inelastically can be collected using a subsequent set of lenses, apertures and a detector. A simplified schematic of a TEM illumination system is shown in Fig.2.1:

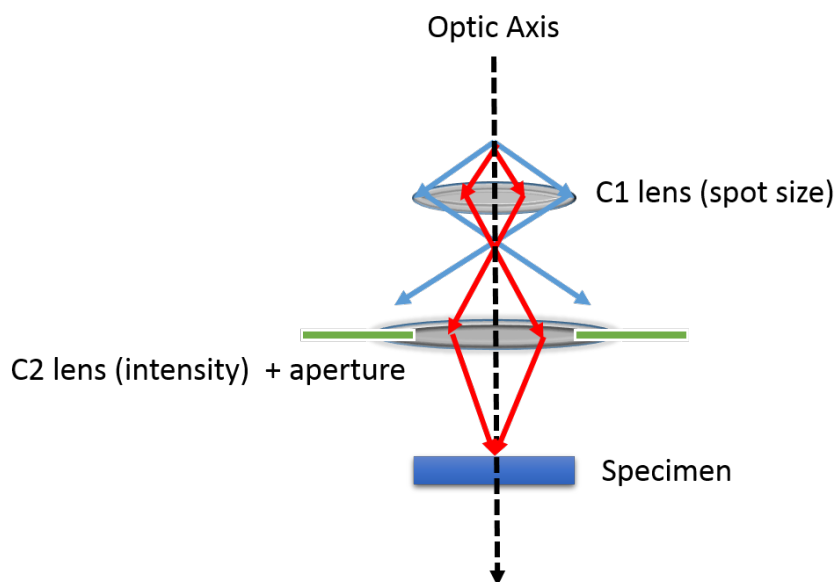


Fig. 2.1 Simplified TEM illumination system.

It is important to consider the range of electron-specimen interactions which occur as the high energy electron beam impacts the sample. These interactions can be divided into two main categories according to whether the electron kinetic energy is either conserved or not during the interaction, known as elastic or inelastic respectively. Different elastic and inelastic signals produced by the electron-specimen interaction are illustrated in Fig.2.2.

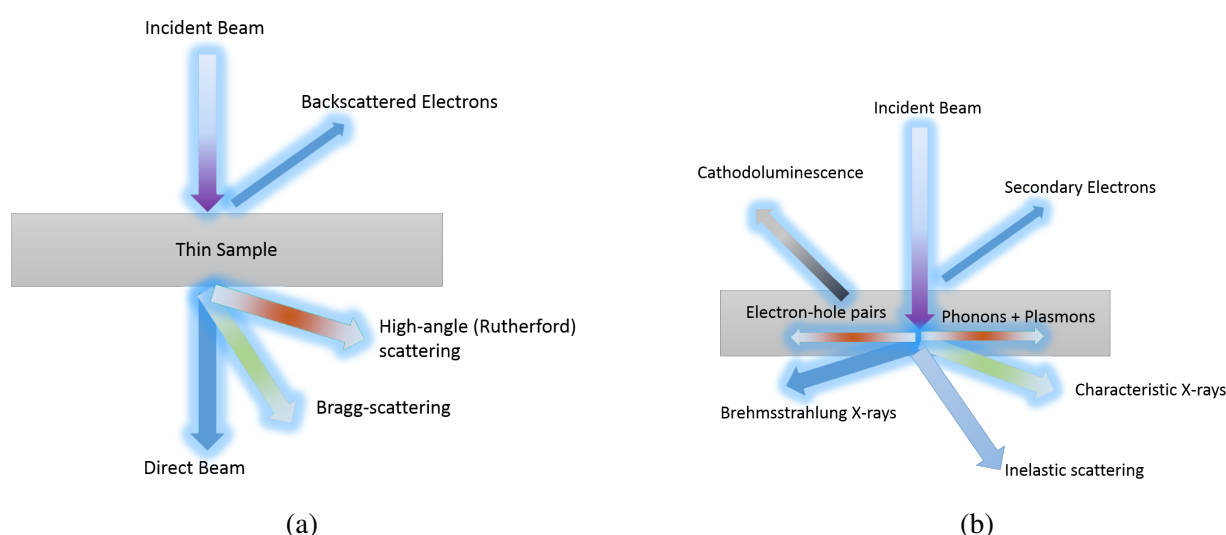


Fig. 2.2 a) Elastic and b) inelastic interactions for a high energy electron beam incident on a thin sample.

Fig.2.2 a) illustrates the importance of sample thickness in TEM. Without a thin specimen, the forward scattered signals such as high-angle and bragg-scattered electrons as well as the direct beam are unavailable. Given the diversity of scattering interactions which can occur throughout the sample and contribute to the final signal, different apertures and detectors must be used to extract useful information. The following sections will introduce the different TEM techniques used in this report and their underlying principles.

2.1.1 Conventional Transmission Electron Microscopy

2.1.1.1 Electron Diffraction

Electron diffraction is the basis for many TEM techniques as it provides local crystallographic specimen information. The process of diffraction occurs for electrons due to their dual nature as both particles and waves. A beam of electrons can thus be interpreted as a plane wave: the incidence of this plane wave on the specimen results in the scattering of the electrons by atoms through the Coulomb interaction, diffracting the wave in a manner described by Bragg's law. This is given by Eq. 2.1.

$$n\lambda = 2d_{hkl}\sin\theta_B \quad (2.1)$$

where n is an integer, λ is the wavelength of the plane wave, d_{hkl} is the crystal plane spacing described by the Miller indices h, k and l and θ_B is the angle between the plane normal and the scattered wave, also known as the Bragg angle.

Understanding of the diffraction patterns observed in TEM requires consideration of the reciprocal lattice of the crystal. The reciprocal lattice is defined as the Fourier transform of the crystal lattice, as such the relation of the real-space unit-cell lattice points \mathbf{a} , \mathbf{b} and \mathbf{c} to their reciprocal lattice counterparts \mathbf{a}^* , \mathbf{b}^* and \mathbf{c}^* can be described as:

$$\mathbf{a}^* = \frac{\mathbf{b} \times \mathbf{c}}{V_c}, \mathbf{b}^* = \frac{\mathbf{c} \times \mathbf{a}}{V_c}, \mathbf{c}^* = \frac{\mathbf{a} \times \mathbf{b}}{V_c} \quad (2.2)$$

where V_c is the volume of the unit cell and is given by the relation"

$$V_c = \mathbf{a} \cdot \mathbf{b} \times \mathbf{c} \quad (2.3)$$

As such one can define lattice points in reciprocal space which are normal to the plane (hkl) in the real lattice as:

$$\mathbf{r}^* = h\mathbf{a}_1^* + k\mathbf{a}_2^* + l\mathbf{a}_3^* \quad (2.4)$$

where \mathbf{a}_1 , \mathbf{a}_2 , \mathbf{a}_3 and \mathbf{c} are the four hexagonal unit-cell vectors as shown in Fig.2.3.

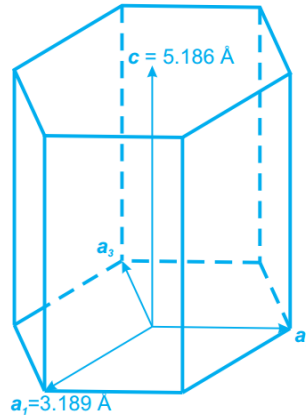


Fig. 2.3 Hexagonal GaN lattice in real space with unit-cell vectors defined. Adapted from [68].

Considering a beam of electrons of wavelength λ incident on a crystal lattice, one can define a sphere in reciprocal space with radius $\frac{1}{\lambda}$ which describes the scattering of the

electron beam known as the Ewald sphere. The intersection of the Ewald sphere with lattice points in reciprocal space represent the diffraction spots which can be observed. Typically, the geometry of the TEM specimen results in elongated reciprocal lattice points known as rel-rods. This elongation allows the Ewald sphere to intersect a greater number of 'points', even with slight deviations to the Bragg condition. The scattering vector \mathbf{K} can thus be described as:

$$\mathbf{K} = \mathbf{k}_D - \mathbf{k}_I = \mathbf{g} + \mathbf{s} \quad (2.5)$$

where \mathbf{k}_D and \mathbf{k}_I are the diffracted and incident beam wavevectors respectively, \mathbf{g} is a reciprocal lattice point intersecting the Ewald sphere and \mathbf{s} is the excitation error, which describes how far the scattering deviates from the exact Bragg diffraction condition. These concepts are shown schematically in Fig.2.4.

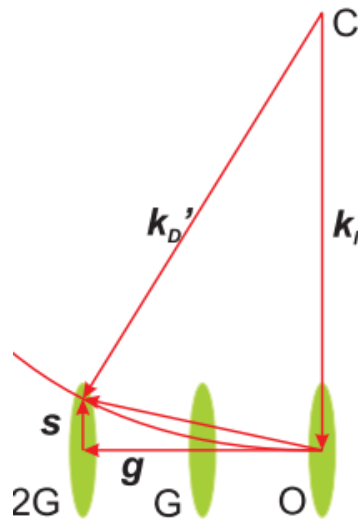


Fig. 2.4 Intersection of the Ewald sphere centered at C with reciprocal lattice rel-rods. Adapted from [68].

Due to the small value of λ (typically picometres), the radius of the Ewald sphere tends to be large relative to the reciprocal lattice spacing, meaning the surface of the sphere is approximately planar relative to the reciprocal lattice rods thus resulting in several spots being observed even in cases where the incident beam is parallel to the zone axis.

2.1.1.2 Diffraction Contrast Imaging

Diffraction contrast imaging is a conventional TEM technique which exploits differing Bragg diffraction conditions in different regions of the sample to create contrast in an image. Image

contrast can be obtained either through bright field (BF) or dark field (DF) imaging, these are shown schematically in Fig 2.5 below:

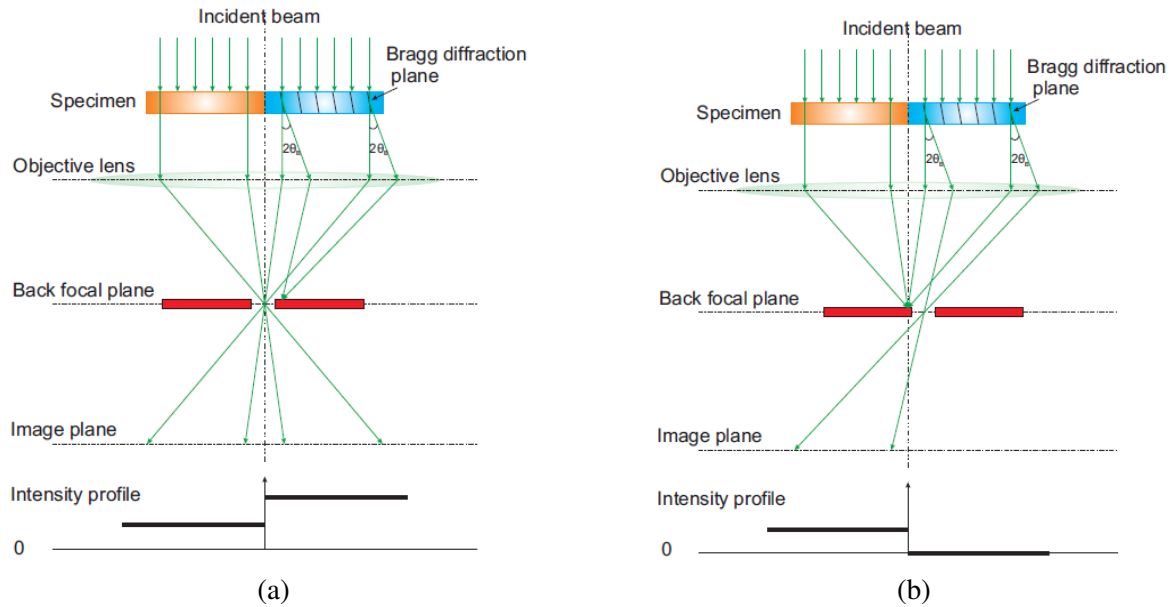


Fig. 2.5 a) Bright-field and b) dark-field imaging [68].

The blue region is shown to satisfy the Bragg diffraction condition for the incident beam whereas the orange region does not. In the case of BF imaging the direct beam is used to generate the image, and as a result the intensity from the orange region is higher than that of the blue region. On the other hand, in DF imaging the diffracted beam is used and the direct beam blocked, resulting in an inverted intensity profile. Barring other electron-specimen interactions such as absorption, the contrast between the BF and DF images is complementary [69].

Figures 2.5 a) and b) demonstrate that the insertion of an aperture at the back-focal plane (BFP) of the objective lens allows for the selection between BF and DF imaging. Without the objective aperture the image consists of a superposition of BF and DF images with a single DF image for every diffracted beam. In order to ensure the diffracted beam is at the optic axis where spherical aberration of the objective lens is less pronounced the incident beam is often tilted, a practice known as centred dark field (CDF) imaging. As dislocations in a crystal structure can be found near strained crystal planes, these will result in diffraction contrast in BF or DF images. However it is important to consider that many diffraction spots can be observed in the electron diffraction pattern, which is undesirable for BF or DF contrast imaging. As such the optimal conditions for are defined as the two-beam condition, in which only one set of planes satisfies the Bragg condition [69], resulting in two beams: the

direct beam and the sole diffracted beam. Under the two-beam condition, image contrast is optimized and the intensity of the two beams can be analytically calculated using the Howie-Whelan equations [69] to deliver detailed information concerning the specimen through the interpretation of contrast in the image.

2.1.1.3 Weak-Beam Dark-Field Microscopy

An alternative technique known as weak-beam dark-field (WBDF) imaging is often used to image dislocations. As indicated by its name, the technique uses a weakly excited beam to form a DF contrast image. A particular diffraction vector \mathbf{g} associated with a specific set of planes hkl is chosen as in regular on-axis DF imaging. The specimen is then tilted to introduce a large excitation error $s_{\mathbf{g}}$ and bring the first diffraction order G onto the optic axis, in doing so the $3G$ reflection satisfies the Bragg diffraction and appears brighter, whilst the zero-order beam is very weak as shown schematically below:

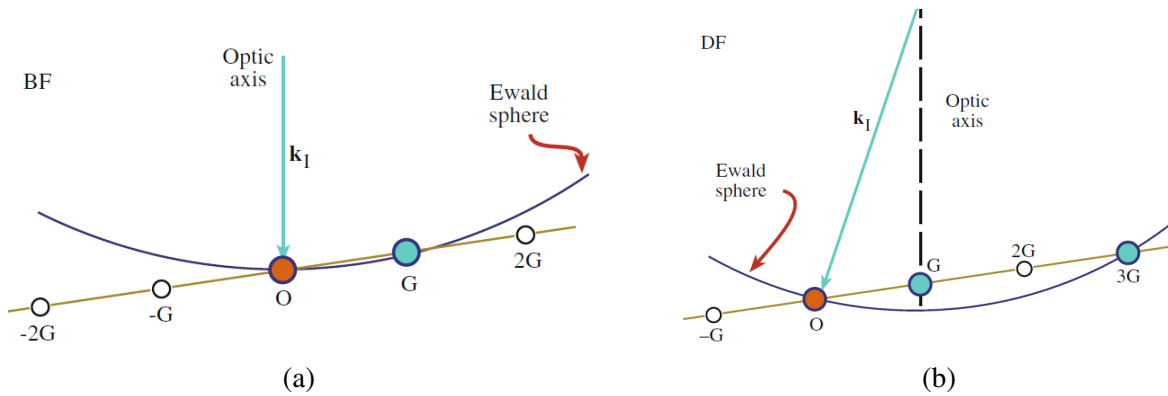


Fig. 2.6 Specimen is tilted from a) to b) for the g - $3g$ condition [69].

As such, most of the lattice planes within the specimen are rotated away from the Bragg condition but near the cores of dislocations these are bent back and appear as high intensity features. The high contrast enables highly detailed imaging of dislocations [69], as shown in Fig.2.7.

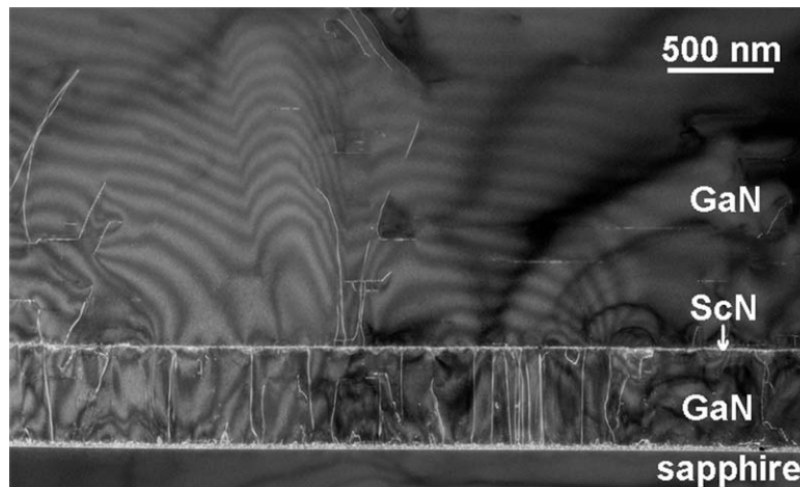


Fig. 2.7 WDBF imaging of dislocations [70].

2.1.2 Scanning Transmission Electron Microscopy

Scanning transmission electron microscopy (STEM) differs from conventional TEM in that a converged electron beam is utilised to generate an image, as opposed to a parallel incident beam as described in section 2.1.1. The convergence of the electron beam generates a probe which can be as small as several angstroms, which is focused and scanned across the sample. Each pixel in the image generated by this technique is acquired from the probe in a separate position by collecting radiation emitted from the sample.

A critical parameter in STEM is the brightness of the source which determines the current in the electron probe. Consequently, field emission guns (FEG) are favoured over thermionic guns such as tungsten or LaB_6 for use in STEM. Another factor which contributes to the preference for FEGs in STEM is the increased spatial localisation of the electron emission compared to thermionic sources, which allows for a smaller probe.

The probe in STEM is a demagnified image of the crossover from the electron gun. The figure below illustrates how a strong gun lens results in a cross over close to the gun such that fewer electrons travel through the collector aperture, leading to a smaller probe with a lower current on the sample.

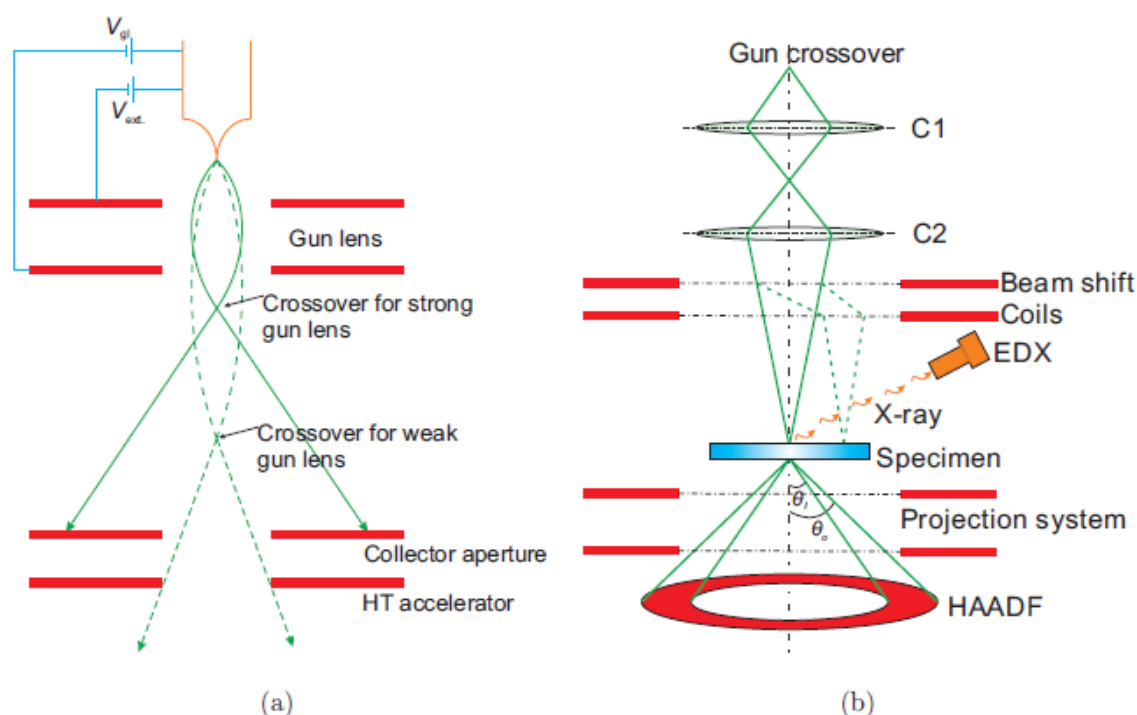


Fig. 2.8 Illustration of a) the FEG source and gun lens b) the column of a STEM with a HAADF for z-contrast imaging and EDX detector [68].

As different STEM techniques such as high-angle annular dark-field (STEM-HAADF) imaging, energy dispersive X-ray spectroscopy (STEM-EDX) or convergent beam electron diffraction (STEM-CBED) imaging will require different probes for optimal results, the strength of the gun lens allows for the adjustment of the required parameters [69]. STEM-HAADF is a STEM technique which allows for what is commonly known as Z-contrast imaging, or imaging by atomic number. The basic principle of operation relies on the fact that electrons scattered by atoms at relatively large angles are mostly incoherent and can be considered as particles rather than waves. At high angles, the intensity of the scattered electrons is proportional to the square of the atomic number Z [71] thus allowing the determination of atomic number of the material at the location of the probe from the brightness of the collected signal. Thus, the use of a high-angle annular dark-field detector allows for the collection of electrons scattered at high angles as shown in Fig 2.8 b). The magnification in STEM-HAADF imaging is controlled by varying the size of the area scanned by the probe, rather than through the use of lenses as in conventional TEM. Strong contrast is typically obtained in HAADF images of III-nitride heterostructures due to the large difference in atomic numbers between the group III elements.

2.1.3 Energy-Dispersive X-ray spectroscopy

Electron-induced X-ray emission allows for the characterisation of sample composition. The high-energy electron beam incident on the sample in TEM can excite an electron from an inner orbital, generating a hole. As electrons from higher energy orbitals relax into this vacancy a characteristic X-ray is released, with an energy equal to the difference between the two states involved in the relaxation transition.

Siegbahn notation is used to describe characteristic X-ray lines: the first component is the elemental atom emitting the X-ray, second is the electron shell which was ionized to emit the X-ray (K, L or M) and the final component describes the relative intensity of the line for each shell (in order of decreasing intensity: α, β, γ) [72]. These are shown schematically in Fig.2.9

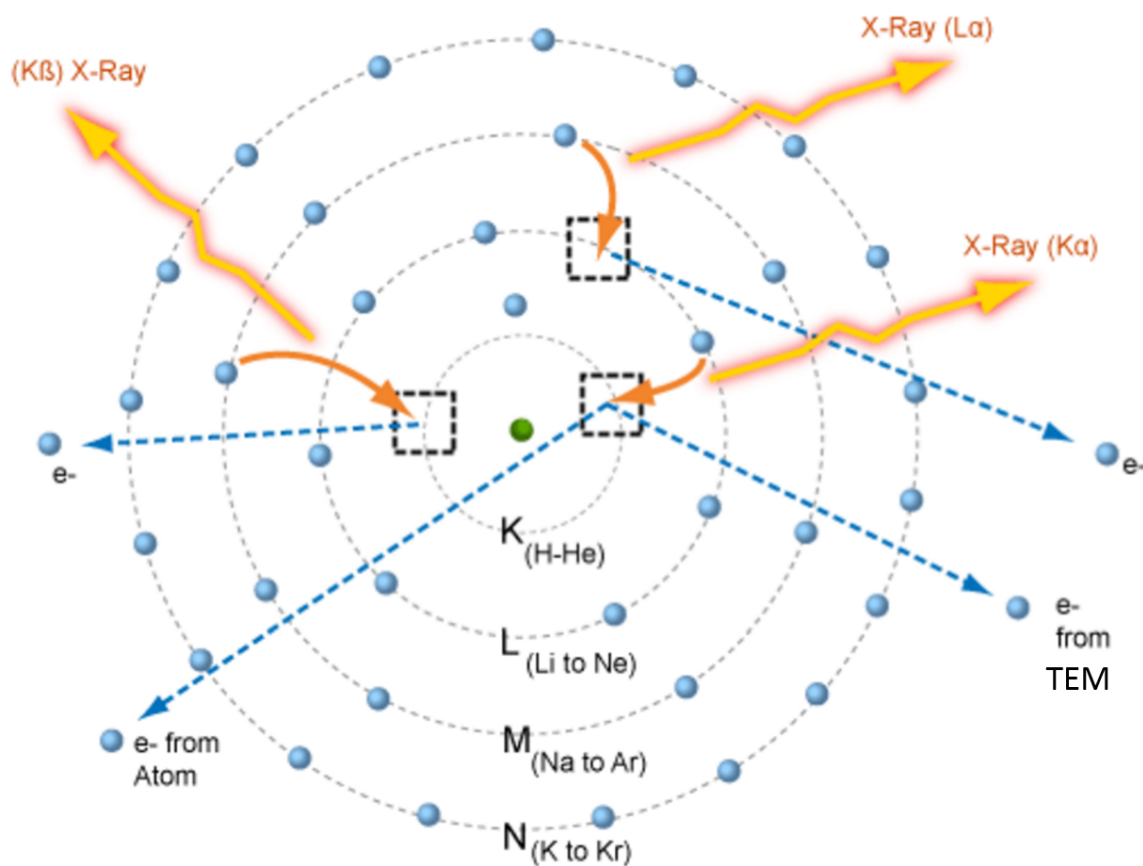


Fig. 2.9 K_{α} , K_{β} , and L_{α} X-rays and their associated electronic transitions. Adapted from [72]

These characteristic X-rays can be collected using an energy dispersive detector, where the X-rays generate electron-hole pairs in a silicon p - i - n junction.

Energy-Dispersive X-ray spectroscopy (EDX) is typically used in STEM mode, where the

electron beam is condensed into a small probe, which leads to the majority of the X-rays being emitted from a small volume in the sample. This enables the acquisition of spatially resolved elemental maps.

2.2 Electron Tomography

TEM provides a plethora of techniques with which to characterise nano-scale structures, however it is often insufficient to ascertain the 3D morphology of complex structures as it deals with projections of the specimen. A typical example of this is network of super-imposed particles in which particles overlapping in the projection may not in fact be in contact in real space [73].

Tomographic reconstruction is a technique that has been widely used to infer 3D volumes from series of 2D projections. A prime example of this is computed axial tomography scanning (CAT-scanning), a technique that has become prevalent in healthcare. The first demonstration of tomography applied to electron microscopy was reported at the MRC laboratory in Cambridge by De Rosier and Klug [74]. Since then, electron tomography (ET) has progressed in leaps and bounds due to advances in technology pertaining to both microscopy and tomographic reconstruction.

The fundamental tenet of tomography lies in the projection theorem developed by Radon at the dawn of the 20th century. The implication of the theorem is that the acquisition of a set of projected images of an object at varying angles can allow for the reconstruction of the full 3D Fourier transform of said object, and consequently the morphology of the object in real space [73] as shown in Fig.2.10.a)

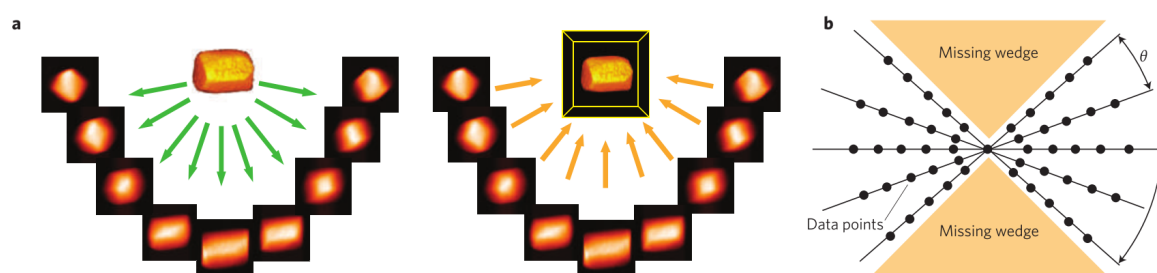


Fig. 2.10 Two-stage tomography process: a tilt series of an object is acquired, then the back projection of these images is used to reconstruct a 3D model of the object [75].

In practical terms, the angular range of the tilt series is an important consideration. A full tilt series acquired between the range $\pm 90^\circ$ allows for minimal anisotropy artifacts. However, typical TEM stage and holder combinations will only allow for a range of $\pm 78^\circ$ due to the

pole-piece gap, leading to a missing wedge of data which results in distortion in the 3D reconstruction [76]. Despite these issues, it has been shown that for tilt ranges larger than $\pm 75^\circ$, the elongation of features due to the missing wedge is below 10% and the volume fraction estimate is within experimental error as other factors such as the interval between images in the series and post-processing can also influence the accuracy of the reconstruction [77].

A common method for tomographic reconstruction is Weighted Backprojection (WBP): this method spreads the specimen mass present in the projection images in equal values amongst computed backprojected rays. This allows for the projection of the specimen back into a reconstructed volume. As the process is repeated for the projection images in the tilt series, the backprojection rays from different images reinforce each other as they intersect at points where the specimen is present [78]. This process typically induces blurring in the reconstructed volume due to an enhancement of low frequencies resulting from the unevenly sampled spatial frequencies in the series [79]. As such, a weighting filter is used to remove the blurring observed in the reconstruction by improving the frequency distribution in Fourier space [79]. An alternative approach to the reconstruction of the specimen volume is to formulate the problem as a system of linear equations, which are solved through the use of iterative methods [80]. This approach is known as the Simultaneous Iterative Reconstruction Technique (SIRT). SIRT performs reconstruction by minimizing the error between projections calculated from the current volume and the experimental projections iteratively [78]. Relative to WBP, SIRT has been shown to yield superior performance under varied experimental conditions and produce the fewest disturbing artifacts in the presence of the 'missing wedge' in the tilt series [81], but is more computationally expensive [78]. The two approaches are shown schematically in Fig.2.11.

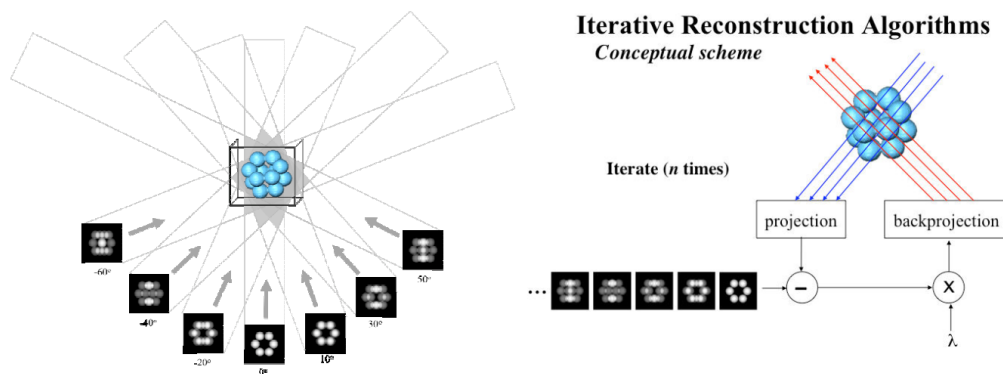


Fig. 2.11 WBP and SIRT reconstruction. Adapted from [78].

In order for the reconstruction to be successful, the signal used in the tilt-series must depend monotonically on the thickness of the sample (or some other physical property) [82]. In the case of HAADF-STEM imaging, this is true as the signal intensity depends both on specimen thickness and atomic number.

2.3 Atomic Force Microscopy

Atomic force microscopy is a non-destructive characterisation technique which employs a sharp tip mounted on a cantilever which is rastered across a sample surface. Tip-surface interactions result in changes cantilever position which are measured using the reflection of laser light reflecting off the cantilever and a four-quadrant photodetector as shown in Fig.2.12 [83].

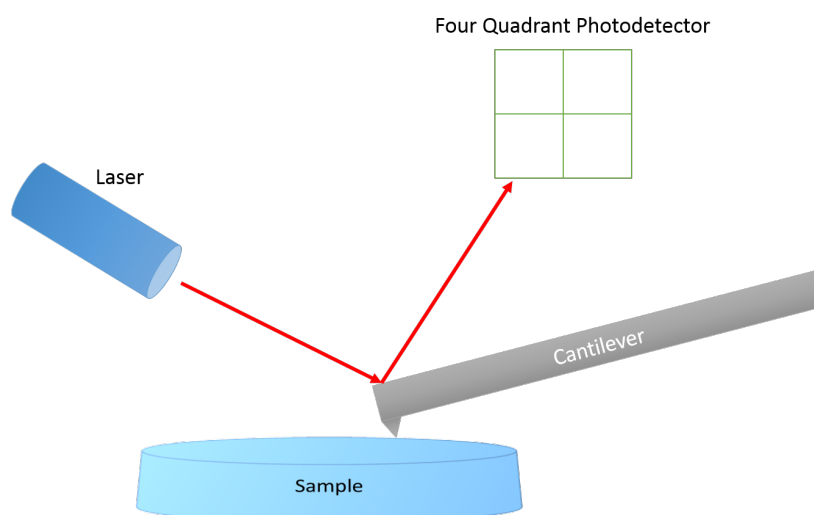


Fig. 2.12 Schematic of an atomic force microscope.

The positioning and movement of the tip is achieved through the use of piezo-electric actuators. In contact mode, a feedback circuit is used to apply a voltage to the piezoelectric crystal in order to maintain a constant tip-sample separation should the tip encounter any features, thus avoiding damage to either the tip or sample. The voltage required to maintain this distance (also known as the setpoint) is registered at each pixel of the scan and is used in conjunction with calibration data to determine a vertical displacement value, thus generating a topographic image [83].

An alternative mode of operation known as tapping mode is often preferred to contact mode. In this mode of operation the tip is made to oscillate close to its resonant frequency by the piezocrystal. Contact between the tip and the sample is achieved at the lowest point of each

oscillation, which damps the oscillation of the tip. The oscillation frequency is maintained by the piezoelectric crystal, thus allowing for the generation of a topographic map. Tapping mode is often preferred to contact mode due to the exclusion of lateral friction which can cause tip wear and sample damage.

The forces experienced by the tip vary depending on the tip-sample separation, as shown in Fig.2.13. Van der Waals forces dominate at large separations attractive the tip to the surface [83]. As the distance is reduced repulsive forces such as hard-sphere repulsion, electron-electron Coulomb interaction and the Pauli-exclusion interaction begin to dominate. The sum of these forces result in cantilever deflection, changing the tip-sample interaction [83].

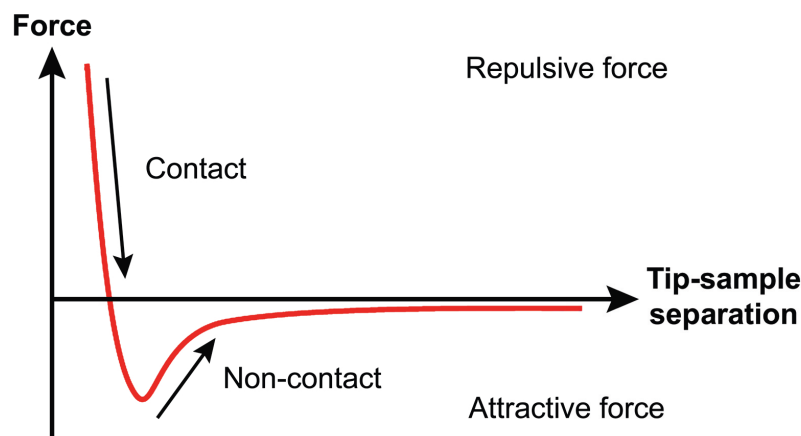


Fig. 2.13 The effect of separation on the tip-sample interaction force [84].

AFM offers excellent vertical resolution limited only by the probes vertical movement and external noise. However, the lateral resolution of this technique is heavily dependent on the shape and size of the tip employed. This is highlighted by Fig.2.14 which depicts a hemispherical tip scanning across a flat-topped island. The apex of the tip is in contact with the surface, but the side of the island also experiences some contact: in this case there is a distinction between the two cases shown in Fig.2.13a) and b) as the error in the measured width of the island varies based on the relative size of the measured object to the tip [83].

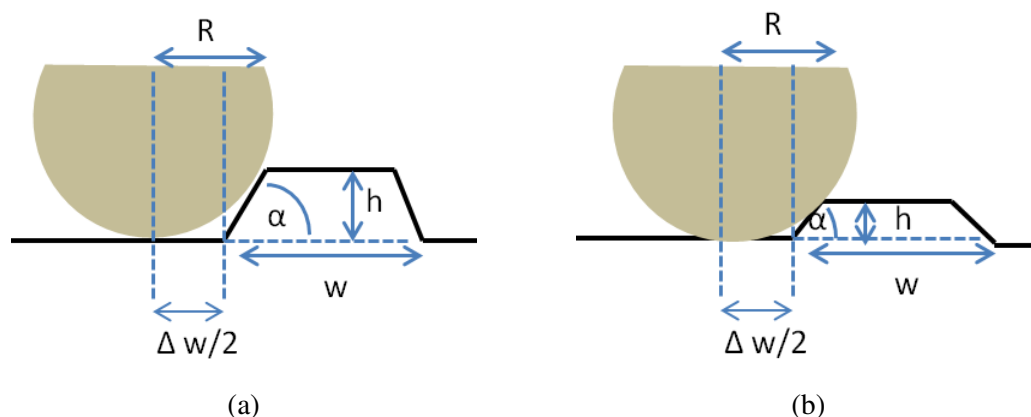


Fig. 2.14 Interaction of a hemisphere with a flat-topped island for the cases a) $h > R(1 - \cos(\alpha))$ and b) $h < R(1 - \cos(\alpha))$ adapted from [83].

Similarly, when measuring depth rather than height the ability of the tip to penetrate into the spaces being measured is also a crucial consideration, as shown in Fig.2.16. Thus, increasing the slope of the tip and minimizing the tip apex are desirable to reduce tip-related measurement artefacts when performing atomic force microscopy [83].

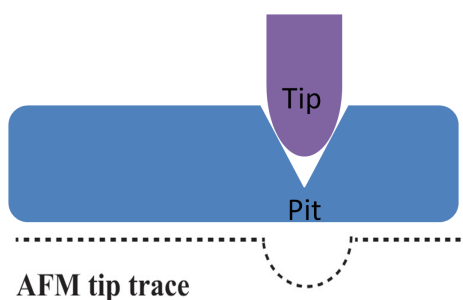


Fig. 2.15 Measurement error in the depth of a pit caused by the finite width of the AFM tip.

2.4 Scanning Electron Microscopy Techniques

A scanning electron microscope (SEM) employs the use of electrons to characterise material morphology and composition. A schematic of a typical SEM design is shown in Fig.2.16.

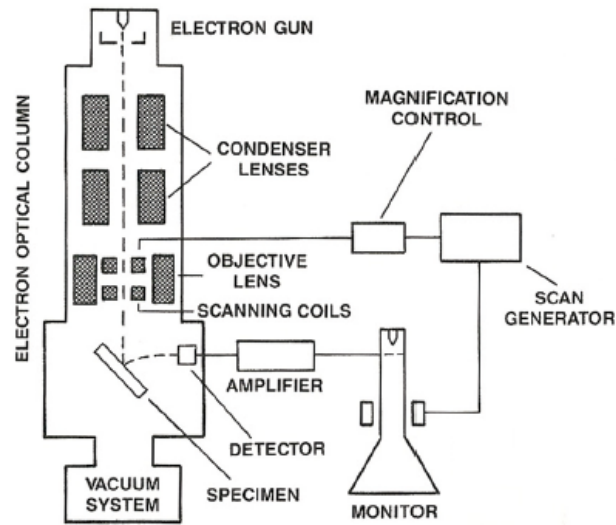


Fig. 2.16 SEM design [85].

The electron gun generates a beam of electrons, typically of energy up to 30 keV. The condenser lenses situated below the gun serve to determine the probe size by adjusting the demagnification of the beam. The objective lens serves to further adjust this demagnification, and is situated directly above the specimen. The scanning coils raster the electron probe across the sample, and the detector thus builds an image of the specimen by collecting various signals which occur due to the electron-specimen interactions [86].

As the beam of electrons interacts with the specimen, various processes occur which generate characteristic signals, as shown in Fig.2.17 and previously discussed in Section 2.1. The volume within the sample which contains the energy deposited by the electron beam is known as the interaction volume, the shape and size of which is determined by both the beam energy and sample composition. Inelastic scattering of the electrons results in the production of signals such as secondary electrons (SEs), Auger electrons and characteristic X-rays [69]. Typically, it is the SEs which are used for imaging in SEMs. Elastic scattering can generate back scattered electrons (BSEs), which are collected through the surface on which the beam is incident. Due to the nature of elastic scattering, BSEs have a strong dependence on atomic, and are can thus be used to produce composition-dependent image contrast [86].

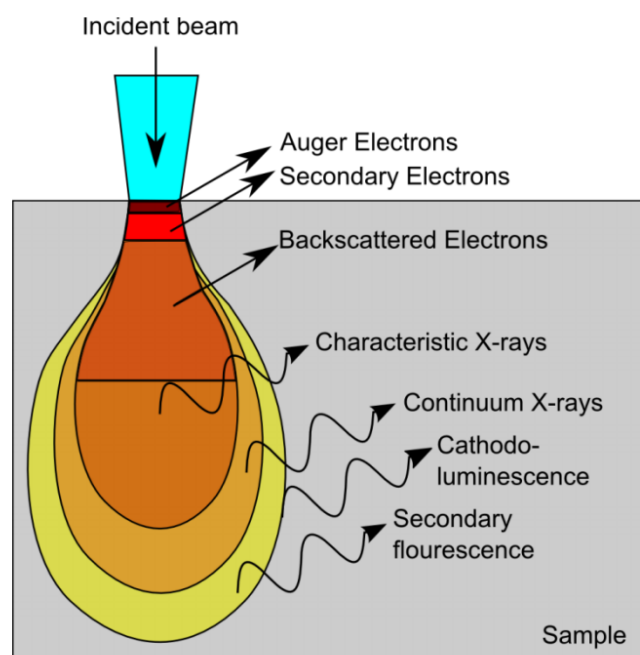


Fig. 2.17 Interaction volumes for different interactions of an electron beam [87].

2.4.0.1 Cathodoluminescence

The absorption of primary electrons in a semiconductor can generate electronic excitations, or electron-hole pairs, with light emission occurring as a consequence of their recombination. This process is known as cathodoluminescence (CL). The electronic transitions which are associated with CL emission require lower energies than those needed to excite X-rays [69].

One of the principal advantages of CL in comparison with photo-excitation spectroscopy techniques used on semiconductors is the limitation of the spatial resolution of the technique by the interaction volume of the electron beam in the material rather than diffraction, which can be considered an intrinsic limitation of most optical far-field techniques [88]. As a result, nanometre-scale characterization of materials can be achieved.

Due to the large number of electron-hole pairs generated within the interaction volume of the impinging electron beam on a bulk semiconductor material, all possible transitions within the material tend to be excited, resulting in the crucial limitation of being unable to selectively excite transitions below a certain energy [88]. Nonetheless, the versatility of CL as a technique has been amply demonstrated in its ability to shed light on the composition of compound materials such as InGaN/GaN structures [89], carrier diffusion length and surface recombination rates [90] and even minority carrier lifetimes [85].

A schematic view of a set-up for CL imaging is shown in Fig. 2.18:

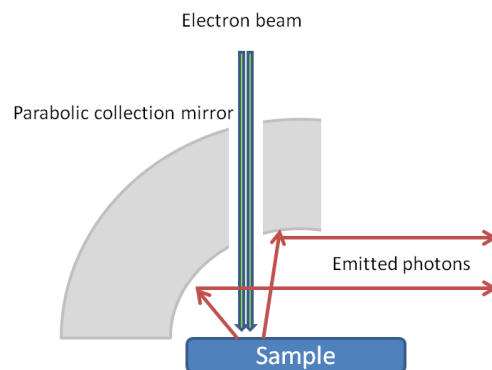


Fig. 2.18 Schematic layout of a CL imaging system.

The electron beam is incident on the sample in the SEM chamber and results in the generation of photons which are collected by a parabolic mirror through a high vacuum feedthrough and coupled into a monochromator. Photomultiplier tubes (PMTs) are the most commonly used detector for this set-up.

The most basic form of CL imaging is known as panchromatic imaging. In this case, the collected light in its entirety is directed to a single detector and the resulting greyscale image intensity is the product of the spectral response of the system and the emission spectrum [88]. An extension of this is the monochromatic imaging mode, in which case only a single band of wavelengths is imaged using a band-pass filter or spectrometer [88].

CL hyperspectral imaging, or CL wavelength imaging is an extension of the aforementioned technique whereby a full luminescence spectrum is recorded at each point during a beam scan, enabling the construction of a spatially and spectrally resolved data set.

In the set-up shown in Fig 2.18, a semi-paraboloidal mirror allows emitted photons to be collected over close to the entire hemisphere. In this case, the beam is scanned across the sample in order to achieve CL hyperspectral imaging, however a number of drawbacks are inherent to this collection geometry:

- The position of the mirror requires a large working distance and can obscure the optical element thus compromising the imaging capabilities of the microscope.

- The small distance between the sample and mirror imposes a restriction on the extent to which the sample can be tilted, which can be an issue in the examination of three-dimensional structures.

- The *étendue* of the system imposes a strict compromise between the field of view of the microscope and the collection efficiency at the spectrometer [88].

In an effort to overcome these limitations, CL hyperspectral imaging systems have been developed, whereby light collection is achieved using an objective placed perpendicular to the electron beam as shown below in Fig 2.19. By allowing the optics to be placed further away from the sample, a far shorter working distance can be used, allowing the electron spot to remain small at low accelerating voltages [88].

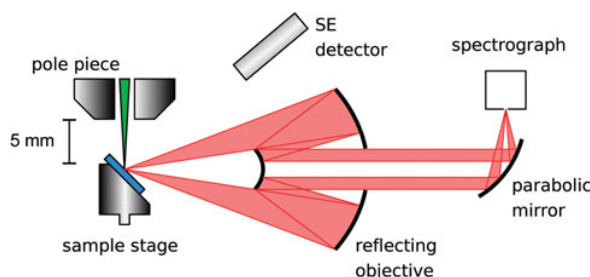


Fig. 2.19 Schematic layout of a CL hyperspectral imaging system [91].

The CL data in this thesis was collected on two separate systems, one employing the collection geometry described in Fig.2.18 and the other shown in Fig.2.19

2.4.0.2 Electron-Beam Induced Current

Electron beam induced current (EBIC) imaging is a technique complementary to scanning electron microscopy. The premise of the measurement is that minority carriers which arise from the incident electron beam of an SEM on a semiconductor junction can diffuse to the junction where they are separated by the built-in field and collected as current by an external circuit (the EBIC amplifier) [92].

Due to the small interaction volumes achievable, EBIC can provide detailed spatial information on minority carrier dynamics. Regions of high signal indicate high collection efficiency and low recombination, for example: the depletion region of a p-n junction appears bright in EBIC imaging. As such EBIC imaging has proven extremely useful in characterising the recombination properties of individual defects across a wide range of semiconductors [93].

2.5 Hyperspectral Electroluminescence Mapping

Hyperspectral electroluminescence (EL) mapping can be used to characterise local variations in EL in optoelectronic devices. The EL mapping data in this thesis was acquired on a modified electron probe micro-analyser (EPMA). The EPMA is fundamentally similar to an SEM with the added functionality of chemical analysis. The primary function of an EPMA

is to acquire elemental analyses at by wavelength-dispersive spectroscopy [94]. In order to perform EL mapping, the electron beam is switched off and a pinhole inserted. A forward bias is then applied to the device being characterised and the stage is moved in order to build up a map of EL emission of the device which is collected by a CCD camera to build up a hyperspectral data set consisting of a full spectrum for each pixel. The spatial resolution of the hyperspectral EL mapping is limited by the magnification of the optical microscope in the EPMA and the pinhole size, in the system used for this work the spatial resolution of the EL measurements was $3\mu\text{m}$ [95].

2.6 Dual Beam FIB-SEM

In this work a dual beam focused ion beam/scanning electron microscope was used to perform sample preparation as well as 'slice and view' tomography experiments. As we have introduced the basic principles behind SEM we will focus on the FIB in this section.

The FIB is an extremely versatile combination of a scanning ion microscope (similar in principle to the SEM but utilising ions rather than electrons) and a precision machining tool[96]. The ions utilised by the FIB are typically Ga^+ , though helium sources also exist . A liquid-metal ion source is used to produce the gallium ions which are focused into a beam and onto the surface of a sample in a similar manner to the SEM using electrostatic lenses and apertures [97]. Due to the complementary nature of FIB and SEM instruments, dual beam FIB/SEM machines have been produced in which the techniques are used synergistically to overcome limitations on individual systems [97]. Aside from a standard electron beam, the FIB-SEM contains an additional gallium ion beam at an angle of 52° to the axis of the electron beam as shown in Fig.2.20

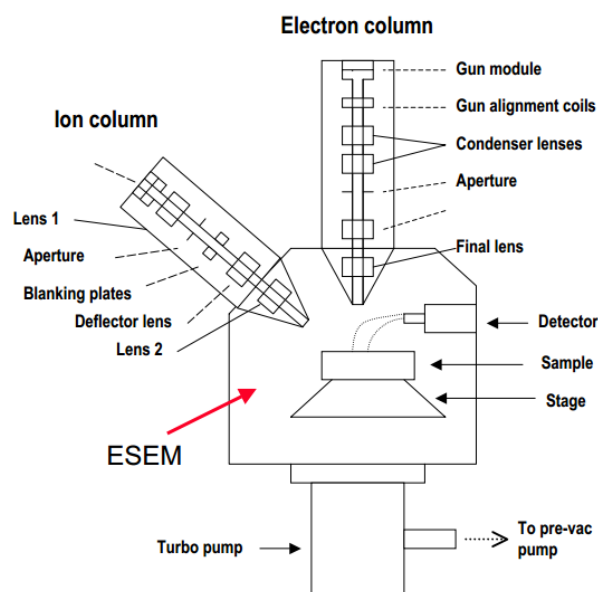


Fig. 2.20 Diagram of a dualbeam FIB-SEM

Due to the large mass of the Ga^+ ions relative to electrons the interaction of the focused ion beam with a sample can cause sputtering of the material, thus allowing for the precise removal of material. Often the SEM is used to monitor the milling process of the FIB as electrons cause negligible damage to the sample relative to the ion beam. Beyond the removal of material, the ion beam can also often be used to deposit material. A gas injection system is typically used to achieve this: a gas containing a metal-organic compound is injected into the chamber where it interacts with the targeted ion-beam at the surface of the sample leading to the heavier metal atoms remaining at the sample surface whilst the organic material is evacuated by the chamber vacuum system. Typically, platinum or carbon can be deposited using this method, though the platinum often contains carbon and other impurities rendering effectively semi-insulating [73].

2.6.1 Sample Preparation

Transmission electron microscopy requires electron transparent samples, typically of a thickness on the order of 100-150 nm. As such the dual beam FIB/SEM allows for site-specific TEM specimen preparation. Unless otherwise stated, all the TEM samples prepared in this work were produced using the FIB/SEM.

The specimen preparation method is shown in Fig.2.21 is as follows:

- A region of interest on the sample surface is identified.
- A protective layer of metal is deposited using the GIS system, first with the electron

beam then with the ion beam.

- Ion milling is used to form trenches on either side of the deposited protective layer
- A probe is then attached to the lamella by connecting the two with ion-beam deposited metal and used to lift the lamella out.
- The lamella is then transferred to a TEM grid, where it is thinned to a suitable thickness.

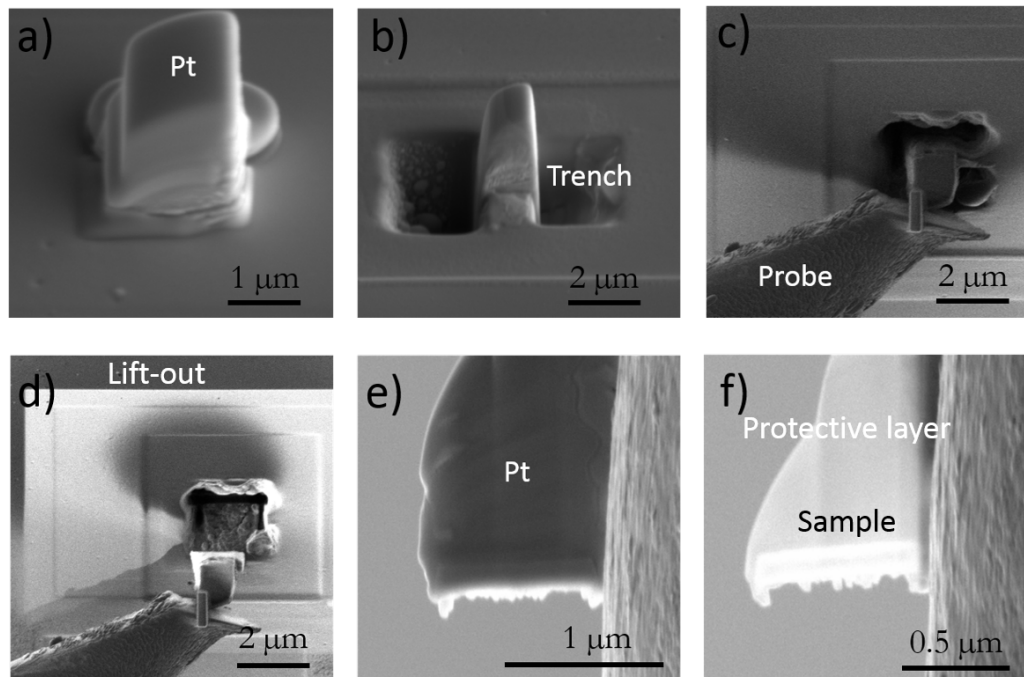


Fig. 2.21 FIB/SEM lamella lift-out and polishing process: a) Protective Pt layer deposition, b) trench milling, c) probe attachment, d) sample lift out e) sample attached onto a TEM grid f) final sample after thinning.

2.6.2 Tomography

FIB/SEM tomography, often referred to as 'slice and view', is a technique which has become relatively widespread in materials and life sciences due to the variety of detection modes available in commercial systems as well as the resolution and volume of material which can be analysed. Typical resolutions that can be achieved (voxel sizes) are in the range 5-10 nm. In FIB/SEM tomography, a small volume of the sample is selected for analysis. This volume is then typically coated with a layer of protective metal in order to prevent ion beam damage. In the experiments described in this thesis, a carbon coating is preferred to the platinum as it provide better contrast in the secondary electron image with GaN. Serial sectioning is then used to analyse the sample: alternating turns of milling and imaging allow for the sequential

erosion of thin layers of material and subsequent imaging as shown in Fig.2.22. In this work we employ only the use of the SE detector for imaging.

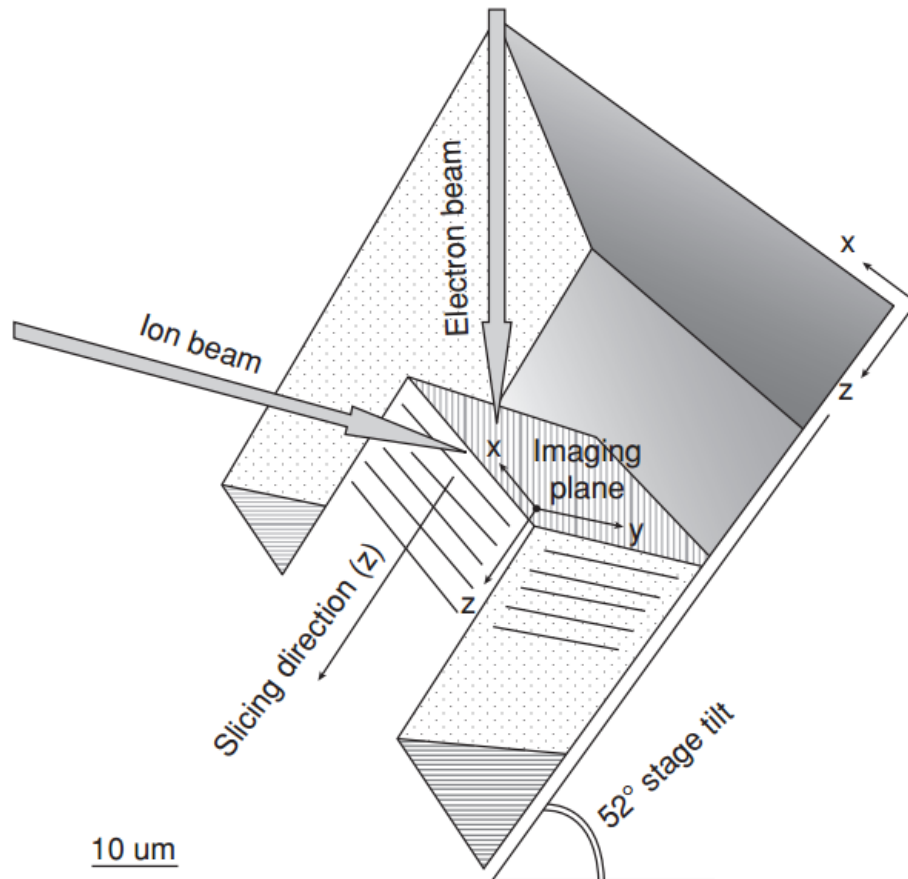


Fig. 2.22 Schematic of sample geometry for serial sectioning in a FIB/SEM instrument [98].

The purpose of serial sectioning is to produce a stack of images which can be transformed into a voxel-based volume data set. As such the thickness of the milled layers should match approximately with the resolution in the imaging plane.

Perhaps the most challenging task in FIB/SEM tomography lies in the extraction of information from the reconstructed 3-D image volume. This procedure, known as 'stack-processing', is very similar to reconstruction protocol used for electron tomography. In this work, the image stack is produced and aligned using the ImageJ [99] plugin StackReg using the 'rigid body' method [100]. Due to the oblique SEM imaging angle of 52°, as discussed in section 2.6, distances measured along the y-axis shown in Fig.2.22 require correction for projection effects. The slice thickness for each layer are derived using the total measured volume divided by the total number of slices [98]. Following this step, thresholding is utilised to binarize the data into the subvolume under examination, and the 'background', this process

is known as segmentation. Accurate evaluation of the subvolume requires high image quality: high contrast and low signal-to-noise ratio are of particular importance [98]. The binary voxel data can be visualized using a wire frame structure calculated from the voxel mask by applying the 'marching cubes' algorithm. Details of the algorithm can be found in [101].

References

- [1] C. J. Humphreys, "USE Solid-State Lighting," *MRS Bulletin*, vol. 33, no. April, pp. 459–471, 2008.
- [2] S. Nakamura, T. Mukai, and M. Senoh, "High-Power GaN P-N Junction Blue-Light-Emitting Diodes," *Japanese Journal of Applied Physics*, vol. 30, no. 12A, pp. 1998–2001, 1991.
- [3] S. Najda, P. Perlin, L. Marona, M. Leszczy, R. Czernecki, S. Watson, A. E. Kelly, A. Malcolm, P. Blanchard, and H. White, "Novel laser diode technology for free-space communications," *SPIE*, pp. 10–12, 2015.
- [4] H. Berlien, H. Breuer, G. Müller, N. Krasner, T. Okunata, and D. Sliney, *Applied Laser Medicine*. Springer Berlin Heidelberg, 2012.
- [5] S. Kako, C. Santori, K. Hoshino, S. Götzinger, Y. Yamamoto, and Y. Arakawa, "A gallium nitride single-photon source operating at 200 K.," *Nature materials*, vol. 5, pp. 887–92, nov 2006.
- [6] S. E. Bennett, "Dislocations and their reduction in GaN," *Materials Science and Technology*, vol. 26, no. 9, pp. 1017–1028, 2010.
- [7] E. T. Yu, X. Z. Dang, P. M. Asbeck, S. S. Lau, and G. J. Sullivan, "Spontaneous and piezoelectric polarization effects in III–V nitride heterostructures," *Journal of Vacuum Science & Technology B: Microelectronics and Nanometer Structures*, vol. 17, p. 1742, 1999.
- [8] I. Vurgaftman and J. R. Meyer, "Band parameters for nitrogen-containing semiconductors," *Journal of Applied Physics*, vol. 94, no. 6, pp. 3675–3696, 2003.
- [9] M. E. Vickers, M. J. Kappers, T. M. Smeeton, E. J. Thrush, J. S. Barnard, and C. J. Humphreys, "Determination of the indium content and layer thicknesses in InGaN/GaN quantum wells by x-ray scattering," *Journal of Applied Physics*, vol. 94, no. 3, pp. 1565–1574, 2003.
- [10] F. Scholz, "Semipolar GaN grown on foreign substrates: a review," *Semiconductor Science and Technology*, vol. 27, p. 024002, feb 2012.
- [11] J. Wu, W. Walukiewicz, K. M. Yu, J. W. Ager, E. E. Haller, H. Lu, and W. J. Schaff, "Small band gap bowing in In_{1-x}Ga_xN alloys," *Applied Physics Letters*, vol. 80, no. 25, pp. 4741–4743, 2002.

- [12] M. D. McCluskey, C. G. Van de Walle, L. T. Romano, B. S. Krusor, and N. M. Johnson, "Effect of composition on the band gap of strained $\text{In}_x\text{Ga}_{1-x}\text{N}$ alloys," *Journal of Applied Physics*, vol. 93, no. 7, pp. 4340–4342, 2003.
- [13] P. G. Moses and C. G. Van De Walle, "Band bowing and band alignment in InGaN alloys," *Applied Physics Letters*, vol. 96, no. 2, pp. 2–5, 2010.
- [14] T. J. Puchtler, A. Woolf, T. Zhu, D. Gachet, E. L. Hu, and R. a. Oliver, "Effect of Threading Dislocations on the Quality Factor of InGaN/GaN Microdisk Cavities," *ACS Photonics*, vol. 2, pp. 137–143, 2015.
- [15] C. X. Ren, "Polarisation fields in III-nitrides: effects and control," *Materials Science and Technology*, vol. 00, no. 0, p. 1743284715Y.000, 2015.
- [16] O. Ambacher and J. Majewski, "Pyroelectric properties of Al (In) GaN/GaN hetero- and quantum well structures," *Journal of physics: ...*, vol. 3399, 2002.
- [17] M. Sumiya and S. Fuke, "Review of polarity determination and control of GaN ," *MRS Internet Journal of Nitride Semiconductor Research*, vol. 9, no. 1, pp. 1–32, 2004.
- [18] C. Wood and D. Jena, *Polarization Effects in Semiconductors: From Ab Initio Theory to Device Applications*. Springer, 2007.
- [19] J. E. R. Miguel, C. J. Gladys, and O. L. César, "Computational calculation of the electronic and magnetic properties of $1 \times 1\text{-MN} / \text{GaN}$ ($\text{M} = \text{V}$, Cr and Mn) multilayers," *International Journal of Physical Sciences*, vol. 9, no. 24, pp. 538–544, 2014.
- [20] V. Fiorentini, F. Bernardini, F. D. Sala, A. D. Carlo, P. Lugli, and T. Vergata, "Effects of macroscopic polarization in III-V nitride multiple quantum wells," *Physical Review B*, vol. 60, no. 12, pp. 8849–8858, 1999.
- [21] S. F. Chichibu, A. Uedono, T. Onuma, B. a. Haskell, A. Chakraborty, T. Koyama, P. T. Fini, S. Keller, S. P. Denbaars, J. S. Speck, U. K. Mishra, S. Nakamura, S. Yamaguchi, S. Kamiyama, H. Amano, I. Akasaki, J. Han, and T. Sota, "Origin of defect-insensitive emission probability in In-containing (Al,In,Ga)N alloy semiconductors.," *Nature materials*, vol. 5, pp. 810–6, oct 2006.
- [22] J. H. Ryou, P. D. Yoder, J. Liu, Z. Lochner, H. S. Kim, S. Choi, H. J. Kim, and R. D. Dupuis, "Control of quantum-confined stark effect in InGaN -based quantum wells," *IEEE Journal on Selected Topics in Quantum Electronics*, vol. 15, no. 4, pp. 1080–1091, 2009.
- [23] M. A. Reshchikov and H. Morko, "Luminescence properties of defects in GaN ," *Journal of Applied Physics*, vol. 97, no. 6, 2005.
- [24] H. Strite, S., Morkoç, " GaN , AlN , and InN : A review," *Journal of Vacuum Science & Technology B*, vol. 10, no. 4, pp. 1237–1266, 1992.
- [25] X. Ning and F. Chien, "Growth defects in GaN films on sapphire: The probable origin of threading dislocations," *Journal of materials ...*, no. 0001, 1996.

- [26] M. a. Moram, C. S. Ghedia, D. V. S. Rao, J. S. Barnard, Y. Zhang, M. J. Kappers, and C. J. Humphreys, "On the origin of threading dislocations in GaN films," *Journal of Applied Physics*, vol. 106, no. 7, p. 073513, 2009.
- [27] R. A. Oliver, M. J. Kappers, C. McAleese, R. Datta, J. Sumner, and C. J. Humphreys, "The origin and reduction of dislocations in Gallium Nitride," *Journal of Materials Science: Materials in Electronics*, vol. 19, pp. 208–214, mar 2008.
- [28] L. Z.-Y. Liu, *Advanced Transmission Electron Microscopy of GaN-based Materials and Devices*. PhD thesis, University of Cambridge, 2011.
- [29] J. Lahnemann, U. Jahn, O. Brandt, T. Flissikowski, P. Dogan, and H. T. Grahn, "Luminescence associated with stacking faults in GaN," *Journal of Physics D: Applied Physics*, vol. 47, no. 42, p. 423001, 2014.
- [30] W. Rieger, R. Dimitrov, D. Brunner, E. Rohrer, O. Ambacher, and M. Stutzmann, "Defect-related optical transitions in GaN," *Physical Review B*, vol. 54, no. 24, p. 17596, 1996.
- [31] Y. Rebane, Y. Shreter, and M. Albrecht, "Stacking Faults as Quantum Wells for Excitons in Wurtzite GaN," *Physica Status Solidi (a)*, vol. 164, no. 141, 1997.
- [32] J. Lahnemann, O. Brandt, U. Jahn, C. Pfüller, C. Roder, P. Dogan, F. Grosse, A. Belabbes, F. Bechstedt, A. Trampert, and L. Geelhaar, "Direct experimental determination of the spontaneous polarization of GaN," *Physical Review B*, vol. 86, pp. 1–5, 2012.
- [33] G. Nogues, T. Auzelle, M. Den Hertog, B. Gayral, and B. Daudin, "Cathodoluminescence of stacking fault bound excitons for local probing of the exciton diffusion length in single GaN nanowires," *Applied Physics Letters*, vol. 104, p. 102102, mar 2014.
- [34] A. Hangleiter, F. Hitzel, C. Netzel, D. Fuhrmann, U. Rossow, G. Ade, and P. Hinze, "Suppression of nonradiative recombination by V-shaped pits in GaInN/GaN quantum wells produces a large increase in the light emission efficiency," *Physical Review Letters*, vol. 95, no. 12, pp. 1–4, 2005.
- [35] S. H. Han, D. Y. Lee, H. W. Shim, J. Wook Lee, D. J. Kim, S. Yoon, Y. Sun Kim, and S. T. Kim, "Improvement of efficiency and electrical properties using intentionally formed V-shaped pits in InGaN/GaN multiple quantum well light-emitting diodes," *Applied Physics Letters*, vol. 102, no. 25, 2013.
- [36] H.-L. Tsai, T.-Y. Wang, J.-R. Yang, C.-C. Chuo, J.-T. Hsu, Z.-C. Feng, and M. Shiojiri, "Observation of V Defects in Multiple InGaN/GaN Quantum Well Layers," *Materials Transactions*, vol. 48, no. 5, pp. 894–898, 2007.
- [37] S. Christopoulos, G. B. H. von Högersthal, a. J. D. Grundy, P. G. Lagoudakis, a. V. Kavokin, J. J. Baumberg, G. Christmann, R. Butté, E. Feltn, J.-F. Carlin, and N. Grandjean, "Room-Temperature Polariton Lasing in Semiconductor Microcavities," *Physical Review Letters*, vol. 98, no. 12, p. 126405, 2007.
- [38] K. J. Vahala, "Optical microcavities.," *Nature*, vol. 424, no. 6950, pp. 839–846, 2003.

- [39] A. F. Jarjour, R. A. Taylor, Robert A. and Taylor, M. J. Kappers, C. J. Humphreys, and A. Tahraoui, "Cavity-enhanced blue single-photon emission from a single InGaN/GaN quantum dot," *Applied Physics Letters*, vol. 91, no. 5, p. 052101, 2007.
- [40] I. Aharonovich, A. Woolf, K. J. Russell, T. Zhu, N. Niu, M. J. Kappers, R. a. Oliver, and E. L. Hu, "Low threshold, room-temperature microdisk lasers in the blue spectral range," *Applied Physics Letters*, vol. 103, no. 2, p. 021112, 2013.
- [41] G. Malpuech, A. Di Carlo, A. Kavokin, J. J. Baumberg, M. Zamfirescu, and P. Lugli, "Room-temperature polariton lasers based on GaN microcavities," *Applied Physics Letters*, vol. 81, no. 3, pp. 412–414, 2002.
- [42] a. Imamoglu, D. Awschalom, G. Burkard, D. P. DiVincenzo, D. Loss, M. Sherwin, and a. Small, "Quantum information processing using quantum dot spins and cavity QED," *Physical Review Letters*, vol. 83, no. 20, pp. 4204–4207, 1999.
- [43] K. Hennessy, a. Badolato, M. Winger, D. Gerace, M. Atatüre, S. Gulde, S. Fält, E. L. Hu, and a. ImamoÄŸlu, "Quantum nature of a strongly coupled single quantum dotâ€cavity system," *Nature*, vol. 445, no. 7130, pp. 896–899, 2007.
- [44] A. C. Tamboli, E. D. Haberer, R. Sharma, K. H. Lee, S. Nakamura, and E. L. Hu, "Room-temperature continuous-wave lasing in GaN/InGaN microdisks," *Nature Photonics*, vol. 1, pp. 61–64, jan 2007.
- [45] S. Chang, N. B. Rex, R. K. Chang, G. Chong, and L. J. Guido, "Stimulated emission and lasing in whispering-gallery modes of GaN microdisk cavities," *Applied Physics Letters*, vol. 75, no. 2, p. 166, 1999.
- [46] E. D. Haberer, R. Sharma, C. Meier, A. R. Stonas, S. Nakamura, S. P. DenBaars, and E. L. Hu, "Free-standing, optically pumped, GaN/InGaN microdisk lasers fabricated by photoelectrochemical etching," *Applied Physics Letters*, vol. 85, no. 22, p. 5179, 2004.
- [47] D. Simeonov, A. Feltin, E. and Castiglia, A. Castiglia, J. F. Carlin, R. Butte, and N. Grandjean, "High quality nitride based microdisks obtained via selective wet etching of AlInN sacrificial layers," *Applied Physics Letters*, vol. 92, no. 17, pp. 2008–2010, 2008.
- [48] E. Yablonovitch, "Inhibited Spontaneous Emission in Solid-State Physics and Electronics Eli," *Physical Review Letters*, vol. 58, no. 20, pp. 2059–2062, 1987.
- [49] S. John, "Strong localization of photons in certain disordered dielectric superlattices," *Physical Review Letters*, vol. 58, no. 23, pp. 2486–2489, 1987.
- [50] K. Ishizaki, M. Koumura, K. Suzuki, K. Gondaira, and S. Noda, "Realization of three-dimensional guiding of photons in photonic crystals," *Nature Photonics*, vol. 7, no. 2, pp. 133–137, 2013.
- [51] A. Tandraechanurat, S. Ishida, D. Guimard, M. Nomura, S. Iwamoto, and Y. Arakawa, "Lasing oscillation in a three-dimensional photonic crystal nanocavity with a complete bandgap," *Nature Photonics*, vol. 5, no. 2, pp. 91–94, 2011.

- [52] Y. Gong and J. Vukovic, "Photonic crystal cavities in silicon dioxide," *Applied Physics Letters*, vol. 96, no. 3, pp. 2009–2011, 2010.
- [53] P. B. Deotare, M. W. McCutcheon, I. W. Frank, M. Khan, and M. Lončar, "High quality factor photonic crystal nanobeam cavities," *Applied Physics Letters*, vol. 94, no. 12, pp. 8–11, 2009.
- [54] M. Notomi, E. Kuramochi, and H. Taniyama, "Ultrahigh-Q nanocavity with 1D periodicity," *Conference Proceedings - Lasers and Electro-Optics Society Annual Meeting-LEOS*, vol. 16, no. 15, pp. 689–690, 2008.
- [55] P. Lalanne and J. P. Hugonin, "Bloch-Wave Engineering for High-Q, Small-V Microcavities," *IEEE Journal of Quantum Electronics*, vol. 39, no. 11, pp. 1430–1438, 2003.
- [56] N. V. Triviño, R. Butté, J.-F. Carlin, and N. Grandjean, "Continuous Wave Blue Lasing in III-Nitride Nanobeam Cavity on Silicon," *Nano Letters*, vol. 15, no. 2, pp. 1259–1263, 2015.
- [57] N. Niu, A. Woolf, D. Wang, T. Zhu, Q. Quan, R. a. Oliver, and E. L. Hu, "Ultra-low threshold gallium nitride photonic crystal nanobeam laser," *Applied Physics Letters*, vol. 106, no. 23, p. 231104, 2015.
- [58] M. Arita, S. Ishida, S. Kako, S. Iwamoto, and Y. Arakawa, "AlN air-bridge photonic crystal nanocavities demonstrating high quality factor," *Applied Physics Letters*, vol. 91, no. 5, p. 051106, 2007.
- [59] W. H. P. Pernice, C. Xiong, C. Schuck, and H. X. Tang, "High-Q aluminum nitride photonic crystal nanobeam cavities," *Applied Physics Letters*, vol. 100, no. 9, 2012.
- [60] A. Bao, "Group III-nitride nanowires Group III-nitride nanowires," *Materials Science and Technology*, vol. 0, no. 0, pp. 1–12, 2017.
- [61] S. Arafin, X. Liu, and Z. Mi, "Review of recent progress of III-nitride nanowire lasers," *Journal of Nanophotonics*, vol. 7, no. 1, pp. 074599–074599, 2013.
- [62] J. C. Johnson, H.-J. Choi, K. P. Knutsen, R. D. Schaller, P. Yang, and R. J. Saykally, "Single gallium nitride nanowire lasers," *Nature materials*, vol. 1, no. 2, pp. 106–110, 2002.
- [63] F. Qian, Y. Li, S. Gradecak, H.-G. Park, Y. Dong, Y. Ding, Z. L. Wang, and C. M. Lieber, "Multi-quantum-well nanowire heterostructures for wavelength-controlled lasers," *Nature materials*, vol. 7, no. 9, pp. 701–706, 2008.
- [64] A. Das, J. Heo, M. Jankowski, W. Guo, L. Zhang, H. Deng, and P. Bhattacharya, "Room temperature ultralow threshold GaN nanowire polariton laser," *Physical Review Letters*, vol. 107, no. 6, pp. 1–5, 2011.
- [65] C.-y. Wu, C.-t. Kuo, C.-y. Wang, and C.-l. He, "Plasmonic Green Nanolaser Based on a Metal-Oxide-Semiconductor Structure," *Nano letters*, pp. 4256–4260, 2011.

- [66] S. Deshpande, J. Heo, A. Das, and P. Bhattacharya, "Electrically driven polarized single-photon emission from an InGa_N quantum dot in a Ga_N nanowire.," *Nature communications*, vol. 4, p. 1675, jan 2013.
- [67] M. J. Holmes, K. Choi, S. Kako, M. Arita, and Y. Arakawa, "Room-Temperature Triggered Single Photon Emission from a III-Nitride Site-Controlled Nanowire Quantum Dot.," *Nano letters*, jan 2014.
- [68] Y. Zhang, *Characterisation of GaN using Transmission Electron Microscopy*. PhD thesis, University of Cambridge, 2008.
- [69] C. B. C. David B. Williams, *Transmission Electron Microscopy*. Springer US, 2009.
- [70] M. a. Moram, Y. Zhang, M. J. Kappers, Z. H. Barber, and C. J. Humphreys, "Dislocation reduction in gallium nitride films using scandium nitride interlayers," *Applied Physics Letters*, vol. 91, no. 15, p. 152101, 2007.
- [71] A. Howie, "Image contrast and localized signal selection techniques," *Journal of Microscopy*, 1979.
- [72] A. M. . M. R. Facility, "Characteristic x-rays." <http://www.ammrf.org.au/myscope/analysis/eds/xraygeneration/characteristic/>.
- [73] G. Divitni, *Electron microscopy studies of photo-active TiO₂ nanostructures*. PhD thesis, University of Cambridge, 2012.
- [74] D. J. De Rosier and A. Klug, "Reconstruction of Three Dimensional Structures from Electron Micrographs," *Nature*, vol. 217, pp. 130–134, 1968.
- [75] P. a. Midgley and R. E. Dunin-Borkowski, "Electron tomography and holography in materials science.," *Nature materials*, vol. 8, no. 4, pp. 271–280, 2009.
- [76] G. Möbus and B. J. Inkson, "Nanoscale tomography in materials science," *Materials Today*, vol. 10, no. 12, pp. 18–25, 2007.
- [77] N. Kawase, M. Kato, H. Nishioka, and H. Jinnai, "Transmission electron microtomography without the "missing wedge" for quantitative structural analysis," *Ultramicroscopy*, vol. 107, no. 1, pp. 8–15, 2007.
- [78] J. J. Fernández, J. I. Agulleiro, A. Martínez, I. García, and F. J. Chichón, "Image processing in electron tomography," *Microscopy: Science, Technology, Applications and Education*, no. Figure 1, pp. 19–28, 2010.
- [79] P. A. Midgley and M. Weyland, "3D electron microscopy in the physical sciences: The development of Z-contrast and EFTEM tomography," *Ultramicroscopy*, vol. 96, no. 3-4, pp. 413–431, 2003.
- [80] P. Gilbert, "Iterative methods for the three-dimensional reconstruction of an object from projections," *Journal of Theoretical Biology*, vol. 36, no. 1, pp. 105–117, 1972.
- [81] P. A. Penczek, "Fundamentals of Three-Dimensional Reconstruction from Projections," pp. 1–33, 2010.

- [82] J. Frank, *Electron Tomography*. Springer New York, 2006.
- [83] R. a. Oliver, “Advances in AFM for the electrical characterization of semiconductors,” *Reports on Progress in Physics*, vol. 71, p. 076501, jul 2008.
- [84] T. Zhu, *Nanoscale Electrical Characterisation of Gallium Nitride*. PhD thesis, University of Cambridge, 2010.
- [85] B. Yacobi and D. Holt, *Cathodoluminescence Microscopy of Inorganic Solids*. Springer US, 1990.
- [86] D. C. Joy, *Scanning Electron Microscopy*. Wiley-VCH Verlag GmbH & Co. KGaA, 2006.
- [87] T. Puchtler, *DEVELOPMENT OF STRUCTURES AND MATERIALS FOR IN-GAN/GAN CAVITY-QUANTUMELECTRODYNAMICS*. PhD thesis, University of Cambridge, 2014.
- [88] P. R. Edwards and R. W. Martin, “Cathodoluminescence nano-characterization of semiconductors,” *Semiconductor Science and Technology*, vol. 26, p. 064005, jun 2011.
- [89] R. W. Martin, P. R. Edwards, K. P. O’Donnell, M. D. Dawson, C.-W. Jeon, C. Liu, G. R. Rice, and I. M. Watson, “Cathodoluminescence spectral mapping of III-nitride structures,” *Physica Status Solidi (a)*, vol. 201, pp. 665–672, mar 2004.
- [90] P. Sercel, H. Zarem, J. Lebens, and L. Eng, “A novel technique for the direct determination of carrier diffusion lengths in GaAs/AlGaAs heterostructures using cathodoluminescence,” *International Electron Devices Meeting*, pp. 285–288, 1989.
- [91] C. L. Paul R. Edwards, Lethy Krishnan Jagadamma, Jochen Bruckbauer and R. W. M. Philip Shields, Duncan Allsopp, Tao Wang, “High-resolution cathodoluminescence hyperspectral imaging of nitride nanostructures,” *Microscopy and Microanalysis*, pp. 1212–1219, 2012.
- [92] N. M. Haegel, *Measurement of Minority Charge Carrier Diffusion Length in Gallium Nitride Nanowires Using Electron Beam Induced Current*. PhD thesis, Naval Postgraduate School, 2009.
- [93] E. Yakimov, “Electron-beam-induced-current study of defects in GaN; experiments and simulation,” *Journal of Physics: Condensed Matter*, vol. 13069, 2002.
- [94] W. Jansen and M. Slaughter, “Elemental mapping of minerals by electron microprobe,” *American Mineralogist*, vol. 67, no. 5-6, pp. 521–533, 1982.
- [95] M. J. Wallace, P. R. Edwards, M. J. Kappers, M. a. Hopkins, F. Oehler, S. Sivaraya, R. a. Oliver, C. J. Humphreys, D. W. E. Allsopp, and R. W. Martin, “Effect of the barrier growth mode on the luminescence and conductivity micron scale uniformity of InGaN light emitting diodes,” *Journal of Applied Physics*, vol. 117, no. 11, p. 115705, 2015.

- [96] T. Ishitani and T. Yaguchi, "Cross-sectional sample preparation by focused ion beam: a review of ion-sample interaction.," *Microscopy research and technique*, vol. 35, no. 4, pp. 320–333, 1996.
- [97] S. Bals, W. Tirry, R. Geurts, Z. Yang, and D. Schryvers, "High-quality sample preparation by low kV FIB thinning for analytical TEM measurements.," *Microscopy and microanalysis : the official journal of Microscopy Society of America, Microbeam Analysis Society, Microscopical Society of Canada*, vol. 13, no. 2, pp. 80–86, 2007.
- [98] L. Holzer, F. Indutnyi, P. Gasser, B. Münch, and M. Wegmann, "Three-dimensional analysis of porous BaTiO₃ ceramics using FIB nanotomography," *Journal of Microscopy*, vol. 216, no. 1, pp. 84–95, 2004.
- [99] W. Rasband, "Imagej," 1997-2016.
- [100] P. Thevenaz, U. E. Ruttimann, and M. Unser, "A pyramid approach to subpixel registration based on intensity," *IEEE Transactions on Image Processing*, vol. 7, pp. 27–41, Jan 1998.
- [101] W. E. Lorensen and H. E. Cline, "Marching cubes: A high resolution 3D surface construction algorithm," *Proceedings of the 14th annual conference on Computer graphics and interactive techniques - SIGGRAPH '87*, vol. 21, no. 4, pp. 163–169, 1987.
- [102] N. K. V. D. Laak, R. A. Oliver, M. J. Kappers, C. J. Humphreys, N. K. V. D. Laak, R. A. Oliver, M. J. Kappers, and C. J. Humphreys, "Role of gross well-width fluctuations in bright , green-emitting single InGaN/GaN quantum well structures Role of gross well-width fluctuations in bright , green-emitting single InGaN / GaN quantum well structures," vol. 121911, no. 2007, pp. 1–4, 2013.
- [103] R. a. Oliver, F. C.-P. Massabuau, M. J. Kappers, W. a. Phillips, E. J. Thrush, C. C. Tartan, W. E. Blenkhorn, T. J. Badcock, P. Dawson, M. a. Hopkins, D. W. E. Allsopp, and C. J. Humphreys, "The impact of gross well width fluctuations on the efficiency of GaN-based light emitting diodes," *Applied Physics Letters*, vol. 103, no. 14, p. 141114, 2013.
- [104] A. Polyakov, N. Smirnov, A. Usikov, A. Govorkov, and B. Pushniy, "Studies of the origin of the yellow luminescence band, the nature of nonradiative recombination and the origin of persistent photoconductivity in n-GaN films," *Solid-State Electronics*, vol. 42, no. 11, pp. 1959–1967, 1998.
- [105] S. Chichibu, a.C Abare, M. Mack, M. Minsky, T. Deguchi, D. Cohen, P. Kozodoy, S. Fleischer, S. Keller, J. Speck, J. Bowers, E. Hu, U. Mishra, L. Coldren, S. DenBaars, K. Wada, T. Sota, and S. Nakamura, "Optical properties of InGaN quantum wells," *Materials Science and Engineering: B*, vol. 59, pp. 298–306, may 1999.
- [106] J. L. Lyons, A. Janotti, and C. G. Van De Walle, "Carbon impurities and the yellow luminescence in GaN," *Applied Physics Letters*, vol. 97, no. 15, pp. 10–13, 2010.
- [107] R. Oliver, M. Kappers, J. Sumner, R. Datta, and C. Humphreys, "Highlighting threading dislocations in MOVPE-grown GaN using an in situ treatment with SiH₄ and NH₃," *Journal of Crystal Growth*, vol. 289, pp. 506–514, apr 2006.

- [108] K. Watanabe, J. R. Yang, S. Y. Huang, K. Inoke, J. T. Hsu, R. C. Tu, T. Yamazaki, N. Nakanishi, and M. Shiojiri, "Formation and structure of inverted hexagonal pyramid defects in multiple quantum wells InGaN/GaN," *Applied Physics Letters*, vol. 82, no. 5, pp. 718–720, 2003.
- [109] M. Shiojiri, C. C. Chuo, J. T. Hsu, J. R. Yang, and H. Saijo, "Structure and formation mechanism of V defects in multiple InGaN/GaN quantum well layers," *Journal of Applied Physics*, vol. 99, no. 7, 2006.
- [110] J. Piprek, *Nitride Semiconductor Devices: Principles and Simulation*. Wiley-VCH, January 20 ed., 2007.
- [111] Y. Li, F. Yun, X. Su, S. Liu, W. Ding, and X. Hou, "Deep hole injection assisted by large V-shape pits in InGaN/GaN multiple-quantum-wells blue light-emitting diodes," *Journal of Applied Physics*, vol. 116, no. 12, p. 123101, 2014.
- [112] Z. Quan, L. Wang, C. Zheng, J. Liu, and F. Jiang, "Roles of V-shaped pits on the improvement of quantum efficiency in InGaN/GaN multiple quantum well light-emitting diodes," *Journal of Applied Physics*, vol. 116, no. 18, p. 183107, 2014.
- [113] D. I. Florescu, S. M. Ting, J. C. Ramer, D. S. Lee, V. N. Merai, a. Parkeh, D. Lu, E. a. Armour, and L. Chernyak, "Investigation of V-Defects and embedded inclusions in InGaN/GaN multiple quantum wells grown by metalorganic chemical vapor deposition on (0001) sapphire," *Applied Physics Letters*, vol. 83, no. 1, p. 33, 2003.
- [114] R. Datta, M. Kappers, M. Vickers, J. Barnard, and C. Humphreys, "Growth and characterisation of GaN with reduced dislocation density," *Superlattices and Microstructures*, vol. 36, pp. 393–401, oct 2004.
- [115] K. Hiramatsu, "Epitaxial lateral overgrowth techniques used in group III nitride epitaxy," *Journal of Physics: Condensed Matter*, vol. 13, pp. 6961–6975, aug 2001.
- [116] B. Beaumont, V. Bousquet, P. Vennéguès, M. Vaille, A. Bouillé, P. Gibart, S. Dassonneville, A. Amokrane, and B. Sieber, "Two-step method for epitaxial lateral overgrowth of GaN," *Physica Status Solidi (A) Applied Research*, vol. 176, no. 1, pp. 567–571, 1999.
- [117] H. El-Ella, F. Rol, D. Collins, M. Kappers, R. Taylor, E. Hu, and R. Oliver, "InGaN super-lattice growth for fabrication of quantum dot containing microdisks," *Journal of Crystal Growth*, vol. 321, pp. 113–119, apr 2011.
- [118] P. Visconti, M. a. Reshchikov, K. M. Jones, D. F. Wang, R. Cingolani, H. Morkoc, R. J. Molnar, and D. J. Smith, "Highly selective photoelectrochemical etching of nitride materials for defect investigation and device fabrication," *Journal of Vacuum Science & Technology B: Microelectronics and Nanometer Structures*, vol. 19, no. 4, p. 1328, 2001.
- [119] C. Youtsey, L. T. Romano, R. J. Molnar, and I. Adesida, "Rapid evaluation of dislocation densities in n-type GaN films using photoenhanced wet etching," *Applied Physics Letters*, vol. 74, no. May 2015, p. 3537, 1999.

- [120] C. Youtsey, L. T. Romano, and I. Adesida, "Gallium nitride whiskers formed by selective photoenhanced wet etching of dislocations," *Applied Physics Letters*, vol. 73, no. 6, p. 797, 1998.
- [121] M. S. Minsky, M. White, and E. L. Hu, "Room-temperature photoenhanced wet etching of GaN," *Applied Physics Letters*, vol. 68, no. 11, pp. 1531–1533, 1996.
- [122] D. Cherns, "The structure and optoelectronic properties of dislocations in GaN The structure and optoelectronic properties of dislocations in," *J. Phys. Condens. Matter.*, vol. 12, p. 10205, 2000.
- [123] H. a. R. El-Ella, F. Rol, M. J. Kappers, K. J. Russell, E. L. Hu, and R. a. Oliver, "Dislocation density-dependent quality factors in InGaN quantum dot containing microdisks," *Applied Physics Letters*, vol. 98, no. 13, p. 131909, 2011.
- [124] S. K. Rhode, M. K. Horton, M. J. Kappers, S. Zhang, C. J. Humphreys, R. O. Dusane, S. L. Sahonta, and M. a. Moram, "Mg doping affects dislocation core structures in GaN," *Physical Review Letters*, vol. 111, no. July, pp. 1–4, 2013.
- [125] M. K. Horton, S. Rhode, S.-L. Sahonta, M. J. Kappers, S. J. Haigh, T. J. Pennycook, C. J. Humphreys, R. O. Dusane, and M. A. Moram, "Segregation of In to dislocations in InGaN.," *Nano letters*, vol. 15, no. 2, pp. 923–30, 2015.
- [126] Y. Xin, E. M. James, I. Arslan, S. Sivananthan, N. D. Browning, S. J. Pennycook, F. Omnes, B. Beaumont, J.-P. Faurie, and P. Gibart, "Direct experimental observation of the local electronic structure at threading dislocations in metalorganic vapor phase epitaxy grown wurtzite GaN thin films," *Applied Physics Letters*, vol. 76, no. 4, p. 466, 2000.
- [127] J. Elsner, R. Jones, P. K. Sitch, V. D. Porezag, M. Elstner, T. Frauenheim, M. I. Heggie, S. Oberg, and P. R. Briddon, "Theory of Threading Edge and Screw Dislocations in GaN," *Physical Review Letters*, vol. 79, no. 19, pp. 3672–3675, 1997.
- [128] O. Ambacher, W. Rieger, P. Ansmann, H. Angerer, T. D. Moustakas, and M. Stutzmann, "Sub-bandgap absorption of gallium nitride determined by photothermal deflection spectroscopy," *Solid State Communications*, vol. 97, no. 5, pp. 365–370, 1996.
- [129] S. Lazar, L. Weyher, J. L. abd Macht, F. D. Tichelaar, and H. W. Zandbergen, "Nanopipes in GaN: photo-etching and TEM study," *The European Physical Journal Applied Physics*, vol. 28, pp. 265–291, 2004.
- [130] N. Vartak, A. Damle-Vartak, B. Richter, O. Dirsch, U. Dahmen, S. Hammad, and J. G. Hengstler, "Cholestasis-induced adaptive remodeling of interlobular bile ducts," *Hepatology*, vol. 63, no. 3, 2016.